

NO-0191 707

LIQUID CARBON(U) MASSACHUSETTS INST OF TECH CAMBRIDGE
M S DRESSELHAUS ET AL. 30 OCT 07 AFOSR-TR-00-0224
F49629-85-C-0147

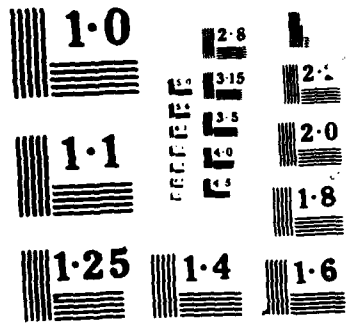
1/1

UNCLASSIFIED

F/O 7/2

NL





2

REPORT DOCUMENTATION PAGE

AD-A191 707 DTIC ELECTE		10. RESTRICTIVE MARKINGS									
13. DECLASSIFICATION/DOWNGRADING SCHEDULE MAR 07 1988		11. DISTRIBUTION/AVAILABILITY STATEMENT Distribution Unlimited									
12. PERFORMING ORGANIZATION NAME(S)		15. MONITORING ORGANIZATION REPORT NUMBER(S) AFOSR-TR-88-0224									
14. NAME OF PERFORMING ORGANIZATION Massachusetts Institute of Technology		16. NAME OF MONITORING ORGANIZATION AFOSR/NE									
17. ADDRESS (City, State and ZIP Code) Rm. 13-3005 MIT, 77 Massachusetts Avenue Cambridge, MA 02139		18. ADDRESS (City, State and ZIP Code) Building 410 Bolling Air Force Base, DC 20332-6448									
19. NAME OF FUNDING/SPONSORING ORGANIZATION AFOSR		20. PROCUREMENT INSTRUMENT IDENTIFICATION NUMBER F49629-85-C-0147									
21. ADDRESS (City, State and ZIP Code) AFOSR/NE ATTN: Dr. Don Ulrich Bolling AFB, DC 20332-6448		22. SOURCE OF FUNDING NOS.									
		<table border="1"> <tr> <th>PROGRAM ELEMENT NO.</th> <th>PROJECT NO.</th> <th>TASK NO.</th> <th>WORK UNIT NO.</th> </tr> <tr> <td>61102F</td> <td>2303</td> <td>A3</td> <td></td> </tr> </table>		PROGRAM ELEMENT NO.	PROJECT NO.	TASK NO.	WORK UNIT NO.	61102F	2303	A3	
PROGRAM ELEMENT NO.	PROJECT NO.	TASK NO.	WORK UNIT NO.								
61102F	2303	A3									
23. TITLE (Include Security Classification) Liquid Carbon											
24. PERSONAL AUTHOR(S) M.S.Dresselhaus, J.Steinbeck											
25. TYPE OF REPORT Reprint		26. TIME COVERED FROM 9-1-86 TO 8-31-87									
		27. DATE OF REPORT (Yr., Mo., Day) October 30, 1987									
		28. PAGE COUNT 30									
29. SUPPLEMENTARY NOTATION											
30. COSATI CODES		31. SUBJECT TERMS (Continue on reverse if necessary and identify by block number)									
FIELD	GROUP	SUB. GR.									
		Liquid Carbon, High Temperature Resistivity of Carbon Fibers, Photoconductivity of Carbon Fibers									
32. ABSTRACT (Continue on reverse if necessary and identify by block number)											
<p>In this brief review article on liquid carbon, the following topics are considered: the phase diagram of carbon, methods for preparing and characterizing liquid carbon, a survey of what is known about the properties of liquid carbon, and models that have been used to account for the properties of liquid carbon. Special emphasis is given to experiments on carbon fibers relevant to determination of the electrical resistivity of liquid carbon.</p>											
33. DISTRIBUTION/AVAILABILITY OF ABSTRACT UNCLASSIFIED/UNLIMITED <input checked="" type="checkbox"/> SAME AS RPT. <input type="checkbox"/> DTIC USERS <input type="checkbox"/>		34. ABSTRACT SECURITY CLASSIFICATION Unclassified									
35. NAME OF RESPONSIBLE INDIVIDUAL Dr. Don Ulrich		36. TELEPHONE NUMBER (Include Area Code) (202) 767-4963									
		37. OFFICE SYMBOL NE									

Liquid Carbon

M.S. Dresselhaus and J. Steinbeck
Massachusetts Institute of Technology
Cambridge, MA 02139

Introduction

Much discussion and controversy [1] has recently been focused on the properties of liquid carbon, formed from the highest melting temperature solid ($T_m \approx 4450\text{K}$). The discussion has centered on the issue of whether liquid carbon is metallic like graphite, or much less conducting (insulating). Graphite is the stable solid from which the liquid is formed at low pressures (see Fig. 1). The interesting physics issues that are raised by this controversy concern the bonding arrangement or coordination of the carbon atoms. If liquid carbon were metallic, it should be an atomic-like liquid, probably similar to liquid Si and liquid Ge (also in Column IV of the periodic table), which are octahedrally coordinated in the liquid phase [2]. On the other hand, if liquid carbon were insulating, it would likely be an exotic molecular liquid, with the bonding requirements of the four valence electrons for each carbon atom fully satisfied. Another possibility that has been proposed is that there is more than one form of liquid carbon, depending on temperature and pressure [3], and perhaps more than one phase of liquid carbon has been experimentally observed [4,5]. Though much is known about carbon chemistry and structure-property relations for various carbons, many uncertainties remain concerning the phase diagram for carbon [6,7].

While this controversy about liquid carbon stimulates scientific interest at seminars and conferences, the properties of liquid carbon may also have practical significance. When a rocket with a carbon coated nose cone reenters the atmosphere, its temperature may get high enough to form liquid carbon; the heat transfer (thermal conductivity) properties of insulating and metallic liquid carbon phases would be expected to differ significantly. As another example, ion beam heating during ion implantation of diamond may melt small regions of the diamond substrate near the surface. The regrowth characteristics of carbon at a diamond interface would therefore be of importance for device applications of ion implanted diamond.

In this brief review, we consider the phase diagram of carbon, methods for preparing and characterizing liquid carbon, a survey of what is known about the properties of liquid carbon, and models that have been used to account for its properties.

The Phase Diagram of Carbon

Although carbon has been studied as a function of temperature and pressure for many years, major uncertainties remain today about the phase diagram of carbon. The most popular phase diagram in use today is the model that stems from the early work by Bundy [8] where he set out to melt graphite under conditions of high temperature and pressure (see Fig. 1). For convenience, we will refer to this phase diagram in the present discussion of liquid carbon.

Since the original work by Bundy [8], many other proposals have been made for the phase diagram of carbon [7]. In addition to the common solid graphite and diamond phases, metallic solid phases have been proposed at very high pressures, [9,10] while at more modest pressures, hexagonal diamond and linearly coordinated carbon phases (carbynes) have been suggested [11]. However, the greatest uncertainty about the carbon phase diagram concerns liquid carbon: whether there is a single liquid phase at low pressures (below ~ 1 kbar pressure), and if so, whether it is metallic or insulating; or whether two or more liquid phases might occur under various conditions of temperature and pressure. A comprehensive and critical review of the various proposed phase diagrams for carbon has recently been made [7] and even more recently updated [12]. The reader is referred to these works for further details.

Preparation of Liquid Carbon

The preparation of liquid carbon involves two key requirements: a suitable crucible and sufficient heat. Since carbon is the highest melting solid, the problem of a suitable crucible has to be met. To avoid contamination, this problem must clearly be solved by melting carbon in a carbon crucible, i.e., forming a puddle of liquid carbon in a carbon (graphite) block. To form the liquid carbon, enough energy ΔH must be supplied to melt the carbon sample

which is initially at temperature T_0 :

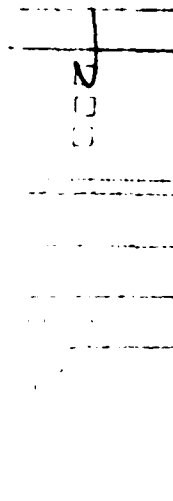
$$\Delta H = \int_{T_0}^{T_m} C(T) dT + \Delta H_m. \quad (1)$$

With a latent heat of melting of $\Delta H_m = 105$ kJ/mole [8] and an increase in enthalpy of 106 kJ/mole in heating from room temperature to the melting point T_m , it is clear that a large amount of energy has to be supplied. The problem of an adequate heat supply is further exacerbated by the high in-plane thermal conductivity of the carbon container. Of all solids, diamond has the highest thermal conductivity ($K = 23$ W/cm-K at room temperature) and that for graphite (in-plane) is only slightly smaller ($K = 19$ W/cm-K). However, by using a graphite container which exploits the low thermal conductivity normal to the layer planes ($K_a/K_c \sim 200$), and by supplying energy fast enough with a pulsed laser or pulsed current source, so that the heat loss by conduction, convection and radiation become negligible on the time scale of the heating pulse, liquid carbon can be formed and studied [13]. As a source for liquid carbon, highly oriented graphite is advantageous because of its high absorption coefficient for laser light [4,5] and its high resistive loss for current pulses [14]. Nevertheless, the pulsed laser technique has produced liquid carbon in graphite [4,5] in diamond [15]. To give some typical magnitudes, with a 30 nsec ruby laser pulse (694 nm) of 2 J/cm^2 intensity, more than 1700 \AA of liquid carbon can be formed over an area of 0.2 cm^2 , and kept in the liquid state for ~ 100 nsec [16]. It should be mentioned that liquid carbon has been produced by direct resistive heating in glassy carbon [17,18] and in graphite at high pressures [8].

In-Situ Characterization

The formation of liquid carbon has been identified both by in-situ measurements in the liquid phase and by measurement of regrowth-induced structure-property modifications in the resolidified phase. As discussed below, in-situ measurements of liquid carbon have not been straightforward, and have been clouded by a number of complications and artifacts. For this reason they have been supplemented by study of the material formed by solidification of the liquid carbon, using several complementary characterization techniques, as discussed below.

Two dominant methods have been used for the in-situ characterization of liquid carbon: time-resolved resistance and time-resolved optical reflectivity



measurements. Of these, the most definitive characterization has been achieved by in-situ measurement of the electrical resistance as a rapid current pulse is passed through a single carbon fiber ($\sim 10\mu\text{m}$ diameter) to form liquid carbon [14], as described below.

With the current pulse heating method, the resistance of a single vapor grown carbon fiber is measured in an ambient N_2 gas or N_2/SF_6 gas mixture as the fiber is heated by a fast pulse ($28\mu\text{sec}$) [14]. The inert gases are used to suppress arcing across the fiber by carriers or ions emitted during the current pulse. The current and voltage across the fiber were monitored as a function of time during the discharge (see inset to Fig. 2). By carrying out measurements on fibers covering a wide range of heat treatment temperatures T_{HT} , the degree of crystallinity in the fibers could be varied; consequently, resistance measurements were made on fibers covering a wide range of transport properties in the solid phase. The most graphitic fibers (see lower trace in Fig. 2) show initially an approximately linear increase in resistance R with time, and reach a maximum resistance value after $\sim 5\mu\text{sec}$ while still in the solid phase. This is followed by a large drop in resistance, as liquid carbon is formed, finally reaching a constant value after $\sim 9\mu\text{sec}$ from the start of the current pulse. We note that the magnitude of the resistivity of liquid carbon is slightly less than that of graphite at room temperature.

Using a finite difference technique, the heat flow equation for graphite is solved to obtain the temperature dependence of the resistance and resistivity for an ohmic heating source term $\sum_i [I(t)]^2 \rho_i(t) / A_i(t)$ where $I(t)$ describes the current pulse, while $\rho_i(t)$ and $A_i(t)$ denote the resistance and cross sectional area of segment i along the fiber length at time t . With this model it is possible to account for the temperature variation along the length of the fiber and to relate the time after the start of the current pulse to the temperature of the fiber.

The results for the temperature dependence of the resistivity $\rho(T)$ obtained from these measurements for fibers with various heat treatment temperatures T_{HT} are given in Fig. 3, where it is seen that independent of the form of $\rho(T)$ in the solid phase below the melting point ($T_m = 4450\text{K}$), the same temperature-independent low resistivity value ($\rho \cong 30 \pm 8\mu\Omega\text{cm}$) is obtained in the liquid phase above T_m [14]. These measurements provide the strongest presently available evidence that liquid carbon is metallic.

Ohmic heating experiments by Bundy [8] show that liquid carbon is also metallic ($\rho \sim 150\mu\Omega\text{cm}$) at elevated pressures $10 < p < 110$ kbar. Also of

relevance are the experiments by Shaner [18] on the ohmic heating of a glassy carbon rod who found a constant value for the resistivity ($\rho \sim 1000 \mu\Omega\text{cm}$) at elevated temperatures and intermediate pressures ($T \sim 6000\text{K}$, $p = 4 \text{ kbar}$). The pressures in the current pulse experiments described above [14] are estimated to be less than 1 kbar. In addition, time-resolved resistivity experiments on pulsed laser heated carbon fibers have been attempted, but their interpretation has been obscured by the observation of photoconductivity phenomena [19].

In contrast to the in-situ resistivity experiments are several recent in-situ optical experiments using pulsed laser heating. The first in-situ reflectivity experiment was carried out using a 30nsec ruby pulsed laser operating at 694 nm for the generation of liquid carbon and a cw He-Ne laser for probing the reflectivity [20].

In-situ pump and probe reflectivity experiments by Malvezzi et al. [5] used a 20 psec Nd:YAG pulsed laser for producing the liquid carbon: after a controlled delay time, the modified surface was examined with probe lasers operating at three different frequencies. The marked decrease observed in the reflectivity R_f above a threshold laser energy density of 0.14 J/cm^2 (see Fig. 4) was interpreted directly in terms of a change in the optical constants, from a semimetallic phase in the solid state to a semiconducting, low conductivity phase for liquid carbon [5].

For pulsed laser experiments in the nanosecond range [20], a decrease in reflectivity was observed and was attributed to particle emission from the surface because of the observed absorption of a light beam just above and parallel to the laser irradiated surface, but not incident on the surface. These particles were assumed to be large enough to absorb and scatter the radiation leaving the sample, thus leading to a reduction in the signal reaching the detector [20]. Numerous ablation studies confirm particulate emission from hot carbon surfaces, and identify the mass and distribution of the emitted C_n clusters [21].

While it is possible to account for the in-situ pulsed nanosecond reflectivity measurements within the framework of a metallic phase for liquid carbon, the particle emission from a molten graphite surface on a 20psec time scale is expected to be negligible [5]. Malvezzi et al. thus argued [5] that particle emission could not alone account for the change in reflectivity observed under 20 psec pulsed laser heating [5]. Although good agreement was obtained between the experimental in-situ reflectivity results at 30nsec and at 20psec with regard to the observation of a threshold for the formation of liquid carbon and a decrease in the reflectivity linked with the formation of liquid carbon, the

different conclusions about the conductivity of liquid carbon remain unresolved at this time.

Some insight has been shed on the complexity of short pulse laser heating experiments by recent time-resolved reflectivity measurements on highly oriented pyrolytic graphite (HOPG) using a ~ 5 psec pulsed laser operating at low energy densities (≈ 0.2 mJ/cm²), three orders of magnitude below the melting threshold for graphite [14]. In these experiments the heating laser was operated at 632.8 μ m and the probe laser at 592.5 nm, and an increase in reflectivity was observed (see Fig. 5) at very short times after the laser pulse. This increase in reflectivity was tentatively identified with the formation of an electron-hole plasma. Later (after ~ 10 psec), a decrease in reflectivity was observed. Of significance in this work is the observation of time dependent phenomena on a 10 psec time scale and of a temperature dependence of the conductivity and reflectivity of graphite at elevated temperatures [14].

The temperature dependence of the resistivity of hot solid carbon may also complicate the interpretation of time resolved resistivity measurements on pulsed laser heated carbon films [22]. While the increased resistance observed by Chauchard et al. [22] after pulsed laser irradiation of graphite may be due to the formation of a quasi-insulating layer of liquid carbon, it may also be possible to account for these observations by artifacts associated with contributions from layers of hot solid carbon and vaporization effects resulting in loss of material from the surface. While pulsed laser melting may be an attractive method for forming liquid carbon, quantitative interpretation of the in-situ experiments is difficult.

Resolidification Studies of Liquid Carbon

For the pulsed current heating experiments, the carbon fibers are usually destroyed upon melting. Thus pulsed laser heating is a more appropriate method for producing liquid carbon when the goals of the experiments are the characterization of the material formed by the recrystallization of liquid carbon. Such characterization experiments have been significant in demonstrating the formation of liquid carbon and in inferring some of the properties of liquid carbon. There are basically four characterization techniques that have been used to study carbon samples subsequent to recrystallization from the liquid state, and these are described below.

Rutherford backscattering/ion channeling measurements [4] show that above a threshold laser energy density, a disordered near-surface layer is formed with a sharp interface to the highly crystalline material of the original highly oriented pyrolytic graphite (HOPG) sample (Fig. 6a), consistent with the prior formation of liquid carbon by pulsed laser irradiation [4]. The rise in the backscattering yield near the surface is identified with disorder in the recrystallized carbon that blocks the ion channels along the c-axis of the graphite crystal substrate. The unique information provided by the Rutherford backscattering/ion channeling experiments is the thickness of the disordered near-surface layer as a function of the laser energy density E_l (Fig. 6b). The thickness of this disordered layer d_d is identified with the maximum thickness of the liquid carbon layer d_l that had been formed by the laser pulse minus the thickness of the near surface layer that had vaporized d_v , so that $d_d = d_l - d_v$.

Using a finite difference method to solve the heat equation for a pulsed laser source term, the thicknesses of the molten and vaporized layers (d_l and d_v) have been calculated [13,16]. The good fit that is obtained for d_d is shown in Fig. 6b for the melting graphite with 30 nsec pulses at 694 nm and with 25 nsec pulses at 248 nm. In addition, the fit of the model calculation to the experimental results give the melting temperatures T_m , and the vaporization temperature T_v (see Table 1). To achieve the high thermal conductivity K necessary to account for the large amount of liquid carbon that is generated and the thickness of the vaporized layer d_v , it is necessary for the liquid to have a very high thermal conductivity. A large thermal conductivity is provided by the nearly free electron model with 4 conduction electrons/carbon atom [16]. Strong support for the validity of this metallic liquid carbon model comes from the fact that the same temperature dependence for the electrical conductivity that is needed to explain the Rutherford backscattering/ion channeling experiments [16] also explains the in-situ resistance measurements on graphite fibers melted by pulsed current heating [14], in the simulation shown as the dotted curves in Fig. 2.

A second experimental technique that has been instrumental in confirming the formation of liquid carbon is Rutherford backscattering on pulsed laser irradiated graphite samples that had previously been implanted with heavy ions at various ion energies to produce markers at various depths [23]. Then as the laser energy density increases, the melt front penetrates further into the sample. When the melt front reaches the implanted marker region, the liquid carbon experiences a large increase in impurity concentration, as the impurities

rapidly diffuse through the liquid. Since the resolidification process after the laser pulse has a high preference for carbon atoms relative to impurity atoms, the impurity concentration in the receding liquid continues to increase greatly. When the solidification front reaches the surface, the residual liquid has its maximum impurity density. The lower boiling point of the impurities leads to a higher vaporization rate of the impurity species. Thus, the marker experiment is expected to show a segregation of impurities at the surface upon solidification of the liquid carbon, together with a general loss in the impurity species through vaporization. Such effects have indeed been observed in Ge and As marker experiments in HOPG [23], as illustrated in Fig. 7. Here it is seen that for a laser energy density of 1.5 J/cm^2 (for a 30 psec ruby laser), an impurity peak at the surface develops. At higher energy densities, more impurities enter the liquid phase and a more pronounced impurity segregation occurs at the surface. By modeling the regrowth process of graphite following the work by Aziz on the regrowth of silicon [24], it was possible to show [13] that the diffusion coefficients for Ge and As in liquid carbon are approximately $D_l \sim 10^{-4} \text{ cm}^2/\text{sec}$, many orders of magnitude faster than in the solid state ($D_s \sim 10^{-10} \text{ cm}^2/\text{sec}$), and of comparable magnitude to the diffusion coefficient of impurities in liquid silicon [24]. The same analysis also yields a value for the segregation coefficient for Ge and As impurities in liquid carbon of $k \simeq 0.17$, where k is defined by $k = C_s/C_L$ where C_s and C_L are the impurity concentrations in the solid and liquid phases at the solid-liquid interface.

The ion-implanted marker experiments can also be used to determine the thickness of the graphite layer that is vaporized d_v as a function of laser energy density E_l . In this case, the impurity is implanted at a depth greater than the penetration of the melt front. Hence, the depth of the implanted marker relative to the surface is determined by the Rutherford backscattering spectra, both before and after pulsed laser irradiation [23].

Further consistency checks for the liquid carbon model are provided by the good agreement between values of d_v vs. E_l as determined directly from the marker experiments described above [23] and the model calculations based on solution of the heat equation [13]. The model calculations for the HOPG samples irradiated with the 30 nsec ruby laser infer that d_v and E_l are proportional above a threshold value of E_l .

Raman spectroscopy provides a third sensitive technique for characterizing the prior presence of liquid carbon [4]. Whereas only the Raman-allowed line at 1580 cm^{-1} due to zone center phonons appears for an HOPG sample prior to the

laser pulse, an additional disorder-induced Raman line appears at $\sim 1360\text{cm}^{-1}$ after the laser pulse, arising from the small size of the graphite crystallites that are formed during the rapid solidification of the liquid carbon, thereby allowing contributions from the Raman scattering to occur for phonons throughout the Brillouin zone [25]. As the energy density of the pulsed laser radiation increases above the threshold value for the formation of liquid carbon, the Raman spectra show an increase in the intensity of the disorder-induced line I_{1360} relative to that for the Raman-allowed line I_{1580} , as well as an increase in the linewidth of both lines, as shown in Fig. 8. However, as the laser energy density is further increased, a remarkable decrease eventually occurs in the relative intensity of the disorder-induced line to the Raman-allowed line given by $R_r = I_{1360}/I_{1580}$ (see Fig. 9). This decrease in R_r is accompanied by a decrease in the linewidth of both Raman lines. This effect is attributed to an increase in the graphite crystallite size, associated with the decreased solidification rate. The slower solidification rate arises from the increased volume of liquid carbon previously formed by the laser pulse [4].

Finally, transmission electron microscopy (TEM) observations show the formation of broad rings going through the (100) and (110) spots of the selected area diffraction patterns after exposure to laser pulses above the melting threshold [4,26]. The broad rings are indicative of the random orientation of the tiny crystallites formed by rapid solidification of the liquid carbon. As the laser energy density is increased well above the threshold level for melting, the rings increase in intensity and eventually sharpen as the crystallite size increases, again associated with the decreasing solidification rate, as described above in connection with the Raman scattering experiments. Of particular interest in connection with the TEM experiment, is the observation at higher laser energy densities of an additional sharp ring in the diffraction pattern at the (002) wavevector [4,26], corresponding to the diffraction from crystallites oriented at right angles to that of the original HOPG sample. This effect is explained by the formation of a more random distribution of crystal orientations as the time for solidification increases.

Scanning electron micrographs of the pulsed laser irradiated surfaces (for both the 30 nsec and 20 psec experiments) show that the rapid solidification gives rise to surface roughness with many local regions exhibiting upheavals of the graphite crystallites near the surface. In addition, many small spheres (diameter $< 0.2\mu\text{m}$) appear to be randomly distributed over the surface after the rapid solidification process. A suggested explanation for the presence of these

spheres is a hydrodynamic droplet formation associated with the minimization of the free energy of the liquid at the surface during rapid solidification [27]. The similarity between SEM, TEM and Raman experimental results on samples previously subjected to the 30 nsec and 20 psec pulsed laser radiation, suggests a similar velocity of the liquid-solid interface during resolidification [26] and is consistent with a single metallic phase for liquid carbon. Nevertheless, the possibility of a second semi-insulating liquid phase remains [5]. Consideration of a shock wave associated with the short laser pulse suggests that liquid carbon is formed by the 30 nsec laser pulse [13] at pressures comparable with the triple point of carbon [28,29].

While it is not possible to conclude that liquid carbon has been formed by pulsed laser heating on the basis of any one of the four widely different experiments discussed above for the characterization of the resolidified material, these experiments collectively provide convincing evidence that liquid carbon had been formed by the pulsed laser radiation [4].

In this connection, it should be emphasized that the same basic model using the finite difference method for solving the heat equation with the same set of temperature-dependent parameters is applied to interpret all the experiments: (1) the in-situ resistivity of carbon fibers melted under pulsed current heating [14], (2) the dependence of the disorder depth of the resolidified graphite on the energy density of the laser pulse as determined by the Rutherford backscattering/ion channeling measurements [16] and (3) the determination of the diffusion properties of the liquid carbon from the observed mass transport of the impurities in the ion implanted marker experiments carried out with the Rutherford backscattering technique [13]. The success of a single basic model in explaining a diverse set of experiments and phenomena lends strong support for a metallic liquid carbon phase at high temperature and low pressure. We summarize the properties of this metallic liquid carbon phase in Table 1.

Properties of Liquid Carbon in the Metallic Phase

From the many diverse experiments that have been performed relevant to the metallic liquid carbon phase, many properties of this liquid metal can be inferred. Once an assignment of 4 valence electrons/carbon atom is made, a number of properties follow directly from the free electron model, such as the electron carrier density n_e , the Fermi wave vector $k_F = (3\pi^2 n_e)^{1/3}$, the Fermi

velocity $v_F = \hbar k_F / m_e$ and the Fermi energy $E_F = \hbar^2 k_F^2 / 2m_e$, where m_e is the mass of the free electron. Numerical values for these properties of liquid carbon are listed in Table 1. Also obtained from the free electron model is the heat capacity of liquid carbon at constant pressure given by

$$C_p = 3R + \pi^2 k_B T R / 2E_F, \quad (2)$$

which yields $C_p = 26$ J/mole-K at T_m ; this value for C_p is to be compared with 28 J/mole-K for the solid phase at T_m [30].

Estimates for the melting temperature $T_m = 4450$ K and the vaporization temperature $T_v = 4700$ K are obtained from the calculation of the disorder depth d_d of the rapidly solidified graphite crystallites, where d_d is measured by the Rutherford backscattering/ ion channeling experiments. This estimate of the melting temperature is in good agreement with thermodynamic studies near the triple point [28,29]. Thermodynamic arguments have been used to evaluate the heat of fusion $\Delta H_m = 105$ kJ/mole [8] and the entropy of fusion $S_m = 2.63$ J/mole-K [29]. From the Clausius-Clapeyron equation, the volume change on melting can be found $\Delta V = \Delta H_m / T_m (dp/dT)$ which becomes 0.14 cm³/g using the value of $(dp/dT) = 1.4 \times 10^8$ dynes/cm²-K [8]. The corresponding densities at the melting point T_m are $\rho_m = 1.54$ g/cm³ for liquid carbon and $\rho_m = 1.97$ g/cm³ for the solid phase [13].

To find the resistivity for a liquid metal, the free electron model must be refined to include correlation effects. Following the work of Ziman [31], Bradley et al. [32], Ferraz and March [3] and Stevenson and Ashcroft [33], the resistivity of the liquid metal is found from the Drude model

$$\rho = m_e v_F / n_e e^2 \ell \quad (3)$$

where the mean free path ℓ is found from the expression

$$\frac{1}{\ell} \propto \frac{1}{2k_F} \int_0^\infty dK K^3 a(K) |V(K)|^2 \Gamma(K). \quad (4)$$

The liquid structure factor $a(K)$ in Eq. (4) is found from the Percus-Yevick model [34], and the pseudopotential $V(K)$ is found from the Heine-Abarenkov model [35], both of which have been calculated for liquid carbon [13] and the results are shown in Fig. 10. The function $\Gamma(K)$ is a correction for the blurring of the Fermi surface since ℓ is of comparable magnitude to the atomic separation of carbon atoms in the liquid phase. Evaluation of the integral for $(1/\ell)$ yields

a value of $\rho_\ell = 40\mu\Omega\text{cm}$ [13], in good agreement with the experimental value of $\rho_\ell = (30 \pm 8)\mu\Omega\text{cm}$ [14]. On the basis of this model, the resistivity of liquid carbon is expected to be independent of temperature since $a(K) \sim 1$, in agreement with the experimental results. Of interest is the low value of the resistivity of liquid carbon compared to that of the solid phase at T_m ($\rho_s \simeq 170\mu\Omega\text{cm}$), which can be explained by the very high carrier concentration in the liquid in comparison with the hot graphite just below the melting temperature.

From the electrical resistivity, the optical constants n and k can be calculated on the basis of the Drude model [13]. Values of the absorption coefficient and reflectivity are given in Table 1 at the frequencies of the pulsed lasers that were used in the pulsed laser melting experiments. Also from knowledge of the liquid structure factor $a(K)$, the compressibility of liquid carbon can be found using the relation

$$\beta_c = a(0)V/k_B T N \quad (5)$$

(see Table 1) [32].

Using the Wiedemann-Franz relation, the thermal conductivity for liquid carbon can be found

$$K_\ell = \pi^2 k_B^2 T / 3e^2 \rho_\ell \quad (6)$$

yielding a value of 2.9 W/cm-K at $T = T_m$. The value of K_ℓ for liquid carbon is much higher than the value of the solid at T_m , where K is highly anisotropic [30] with an in-plane value estimated to be $K_a \sim 1$ W/cm-K at T_m and a much lower c-axis value of $K_c \simeq 0.015$ W/cm-K. It should be noted that the thermal conductivity of liquid carbon is dominated by the electronic contribution, and for the solid phase by the phonon contribution.

Although it has been possible to infer many properties of liquid carbon from indirect experiments and model calculations, detailed experiments are needed to further establish the validity of these models. This remains a challenge for future studies of this highest temperature liquid. Of particular interest would be an experimental determination of the liquid structure factor. Such experiments would also provide important information on the existence of an insulating molecular liquid carbon phase as suggested by picosecond time resolved reflectivity measurements [5].

Studies of the ultra high temperature region of the phase diagram for carbon are both of technological and scientific interest. Current technology in lasers and high speed electronics allow the possibility of experimental advances in the study of liquid carbon. In addition, ab-initio theoretical calculations of such an

interesting and varied phase diagram represent a good test of current numerical techniques. It might be expected that a few surprises and many rewards await the diligent researcher.

Acknowledgments

We greatly appreciate the long term collaboration with Dr. T. Venkatesan (Bell Communications Research Laboratory), Dr. G. Braunstein (Kodak Research Laboratory), and Dr. B. Elman (GTE Research Laboratory) on liquid carbon studies. We would also like to thank our sponsors for their support of this work: the carbon host materials research was supported by NSF Grant #DMR 83-10482; the carbon fiber research was supported by the Advanced Research Projects Agency of the Department of Defense and was monitored by the Air Force Office of Scientific Research under Contract No. F49620-85-C0147.

Table 1. A summary of the properties for the metallic liquid carbon phase [13].

Symbol	Property	Value	Model
n_e	electron density	$3.2 \times 10^{23} \text{cm}^{-3}$	4 electrons/atom
k_F	Fermi wave vector	$2.1 \times 10^8 \text{cm}^{-1}$	Fermi gas
v_F	Fermi velocity	$2.5 \times 10^8 \text{cm/sec}$	Fermi gas
E_F	Fermi energy	17eV	Fermi gas
ρ_m	mass density	1.6 g/cm ³	Clausius-Clapeyron
a	mean C-C distance	2.06Å	-
T_m	melting point	4450K	disorder depth calculation
T_v	boiling point	4700K	vaporization calculation
H_f	Heat of fusion	105 kJ/mole	thermodynamic models
S_f	Entropy of fusion	2.63 J/mole-K	thermodynamic models [29]
ρ	Electrical Resistivity	30μΩ-cm	pulsed current experiments
$K(T)$	thermal conductivity	2.9 W/cm-K	Wiedemann-Franz
$C_p(T)$	heat capacity	26 J/mole-K	Fermi gas
β_c	compressibility	$6.4 \times 10^{-12} \text{Pa}^{-1}$	model calculation
ℓ_p	mean free path	3.4Å	Ziman liquid metal model
R_f	reflectivity	0.82	$\lambda = 694 \text{ nm}$ (Drude)
R_f	reflectivity	0.7	$\lambda = 248 \text{ nm}$ (Drude)
α	absorption coefficient	$1.4 \times 10^6 \text{cm}^{-1}$	$\lambda = 694 \text{ nm}$ (Drude)
α	absorption coefficient	$1.7 \times 10^6 \text{cm}^{-1}$	$\lambda = 248 \text{ nm}$ (Drude)
D_t	Liquid Diffusivity	$10^{-4} \text{cm}^2/\text{sec}$	liquid segregation model
v_p	Interface Diffusive Speed	26 m/sec	liquid segregation model
k	Segregation Coefficient	0.17	liquid segregation model

Figure Captions

Figure 1: The phase diagram suggested by Bundy [8] from experimental data on the high pressure portion of the phase diagram.

Figure 2: Time dependence of the resistance of two carbon fibers (prepared with different heat treatment temperatures) while heated by a 28 μ sec current pulse. The schematic for the experimental arrangement used to heat and melt the graphite fibers is shown in the inset to the lower trace [14]. The dotted curves represent the results of a computer simulation based on solution to the heat flow equation.

Figure 3: The electrical resistivity versus temperature for graphite fibers with $T_{HT} = 1700, 2100, 2300, 2800^\circ\text{C}$. The measured electrical resistivity for liquid carbon is shown. Note that the electrical resistivity for the fiber with $T_{HT} = 1700^\circ\text{C}$ is the only one characteristic of an activated conductivity in the solid state [14].

Figure 4: Transient reflectivity measurements using pulsed laser heating and a pump/probe detection technique. The pump and probe were provided by a 20 psec pulse from a Nd:YAG laser operating at the 532 nm harmonic and the delay time between the pump and probe was varied. The inset shows the short delay time data for low laser energy densities [5].

Figure 5: Time dependent reflectivity of highly oriented pyrolytic graphite heated by a 5 psec laser pulse [633 nm] at laser energy densities far below the threshold for melting. The probe laser is at 592 nm. The inset shows the reflectivity response for the 0.2 mJ/cm² laser energy density over a longer time scale [14].

Figure 6: (a) Rutherford backscattering/ion channeling spectra for 30 nsec pulsed ruby laser irradiated graphite (694 nm). The onset for formation of the disordered layer occurs for a laser energy density of 0.6 J/cm² [4].

(b) Summary of the results of ion channeling spectra on graphite for a 30 nsec pulsed ruby (694 nm) laser and a 25 nsec pulsed KrF (248 nm) laser. The points are experimental and the fits (dashed lines) are made by solution of the heat equation [4,13,16].

Figure 7: Plot of the Rutherford backscattering yield vs. depth (channel number) showing the redistribution of ion implanted germanium in pulsed laser irradiated graphite for several laser energy densities. Note the movement of impurities to the surface using the depth scale shown on the top of the figure [23].

Figure 8: Raman spectra for pulsed irradiated graphite. The spectrum in (a) is for the first and second order Raman peaks in graphite prior to the laser pulse. The spectra in (b) and (c) are the first and second order Raman spectra for graphite irradiated with an energy density of 1.9 J/cm^2 and 3.6 J/cm^2 from a 30 nsec pulsed ruby laser, respectively. For comparison, the spectrum in (d) is for glassy carbon, a disordered graphite with a small crystallite size.

Figure 9: A summary of measurements of the Raman intensity ratio I_{1360}/I_{1580} made with a 20 psec Nd:YAG (532 nm) pulsed laser and a 30 nsec ruby (694 nm) pulsed laser for the laser energy densities shown on the upper and lower scales. Note the relation between I_{1360}/I_{1580} and the in-plane crystallite size L_a shown on the right hand scale [27].

Figure 10: The liquid structure factor $a(k)$ and the pseudopotential function $V(k)$ for a metallic liquid carbon phase [13]. The dashed line denotes the k value of the node in $V(k)$.

References

- [1] Focused Session on Liquid Carbon, *Bull. Am. Phys. Soc.* 32, 608 (1987).
- [2] A. Cutler, "Liquid Semiconductors" (Academic Press, New York, 1977).
- [3] A. Ferraz and N.H. March, *Phys. Chem. Liquid* 8, 289 (1979).
- [4] T. Venkatesan, D.C. Jacobson, J.M. Gibson, B.S. Elman, G. Braunstein, M.S. Dresselhaus, *Phys. Rev. Lett.* 53, 360 (1984).
- [5] A.M. Malvezzi, N. Bloembergen and C.Y. Huang, *Phys. Rev. Lett.* 57, 146 (1986).
- [6] P. Gustafson, *Carbon* 24, 169 (1986).
- [7] F.P. Bundy in "Solid State Physics Under Pressure", ed. by S. Minomura, (Terra Scientific Publishing Co, 1985), p. 1.
- [8] F.P. Bundy, *J. Chem. Phys.* 38, 618 (1963).
- [9] J.A. Van Vechten, *Phys. Rev.* B7, 1479 (1973).
- [10] R. Grover, *High Pressure Sci. and Tech.*, Proc. 7th Int. AIRAPT Conf., Le Creusot, 1979, edited by B. Vodar and P. Marteau.
- [11] A.G. Whittaker, *Science*, 200, 763 (1978); A.G. Whittaker, E.J. Watts, R.S. Lewis and E. Anders, *Science*, 209, 1512 (1980).
- [12] F.P. Bundy, Proc. XI AIRAPT Int. Conf., Kiev (1987) (in press).
- [13] J.W. Steinbeck, Ph.D. Thesis, Massachusetts Institute of Technology, 1987 (unpublished).
- [14] J. Heremans, C.H. Olk, G.L. Eesley, J. Steinbeck and G. Dresselhaus, submitted for publication.
- [15] J.S. Gold, W.A. Bassett, M.S. Weathers and J.M. Bird, *Science* 225, 921 (1984).
- [16] J. Steinbeck, G. Braunstein, M.S. Dresselhaus, T. Venkatesan and D.C. Jacobson, *J. Appl. Phys.* 58, 4374 (1985).

- [17] T. Noda and M. Inagaki, *Bull. Chem. Soc. Jpn.* **37**, 1709 (1964).
- [18] J.W. Shaner, *Bull. Am. Phys. Soc.* **32**, 608 (1987).
- [19] J. Steinbeck, M.S. Dresselhaus, G. Dresselhaus and T. Venkatesan, *Extended Abstracts of the Symposium on Graphite Intercalation Compounds at the Materials Research Society Meeting, Boston* (1986), edited by M.S. Dresselhaus, G. Dresselhaus and S.A. Solin, (Materials Research Society Press, Pittsburgh, PA, 1986), p. 129.
- [20] T. Venkatesan, J. Steinbeck, G. Braunstein, M.S. Dresselhaus, G. Dresselhaus, D.C. Jacobson and B.S. Elman, "Beam-Solid Interactions and Phase Transitions", MRS Symposia Proceedings, eds. H. Kurz, G.L. Olson and J.M. Poate, 1986, vol. 51, p. 251.
- [21] A. Kasuya and Y. Nishina, *Phys. Rev.* **B28**, 6571 (1983).
- [22] F.A. Chauchard, C.H. Lee and C.Y. Huang, *Appl. Phys. Lett.* **51**, 812 (1987).
- [23] G. Braunstein, J. Steinbeck, M.S. Dresselhaus, G. Dresselhaus, B.S. Elman, T. Venkatesan, B. Wilkens and D.C. Jacobson, "Beam Solid Interactions and Phase Transformations", MRS Symposia Proceedings, vol. 51, eds. H. Kurz, G.L. Olson and J.M. Poate (1986), p. 233.
- [24] M.J. Aziz, J.Y. Tsao, M.O. Thompson, P.S. Peercy and C.W. White, *Phys. Rev. Lett.* **56**, 2489 (1986).
- [25] F. Tuinstra and J.L. Koenig, *J. Chem. Phys.* **53**, 1126 (1970).
- [26] J.L. Speck, J. Steinbeck, G. Braunstein, M.S. Dresselhaus and T. Venkatesan, "Energy Beam-Solid Interactions and Phase Transformations", MRS Symposia Proceedings, vol. 51, eds. H. Kurz, G.L. Olson and J.M. Poate (1986), p. 263.
- [27] J. Steinbeck, G. Braunstein, J.S. Speck, M.S. Dresselhaus, C.Y. Huang, M. Malvezzi and N. Bloembergen, *Beam Solid Interactions and Transient Processes, MRS Symposia Proceedings, Boston*, edited by S.T. Pargament, M.O. Thompson and J.S. Williams, (Materials Research Society, 1986), vol. 74, xxx (1987).

- [28] A. Cezairliyan and A.P. Miller, *Bull. Amer. Phys. Soc.* 32, 608 (1987).
- [29] N.A. Gokcen, E.T. Chang, T.M. Poston and D.J. Spencer, *High Temp. Sci.* 8, 81 (1976).
- [30] B.T. Kelly, "Physics of Graphite", (Applied Science Publishers Ltd., London, 1981).
- [31] J.M. Ziman, *Phil. Mag.* 6, 1013 (1961).
- [32] C.C. Bradley, T.E. Farber, E.G. Wilson and J.M. Ziman, *Phil. Mag.* 7, 865 (1962).
- [33] D.J. Stevenson and N.W. Ashcroft, *Phys. Rev.* A9, 782 (1974).
- [34] J.K. Percus and G.J. Yevick, *Phys. Rev.* 110, 1 (1958).
- [35] V. Heine and I. Abarenkov, *Phil. Mag.* 9, 451 (1964).

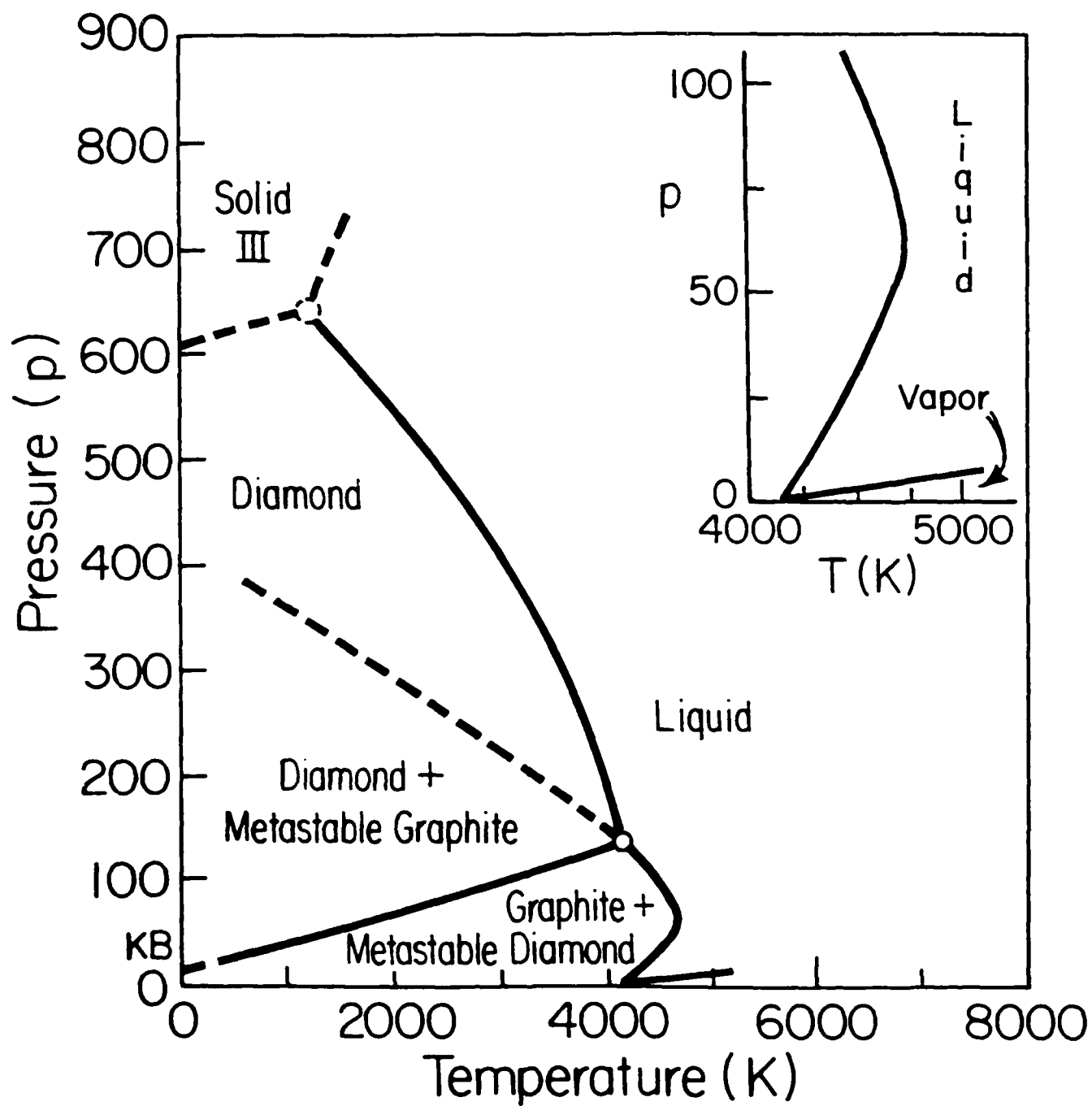


Figure 1: The phase diagram suggested by Bundy [8] from experimental data on the high pressure portion of the phase diagram.

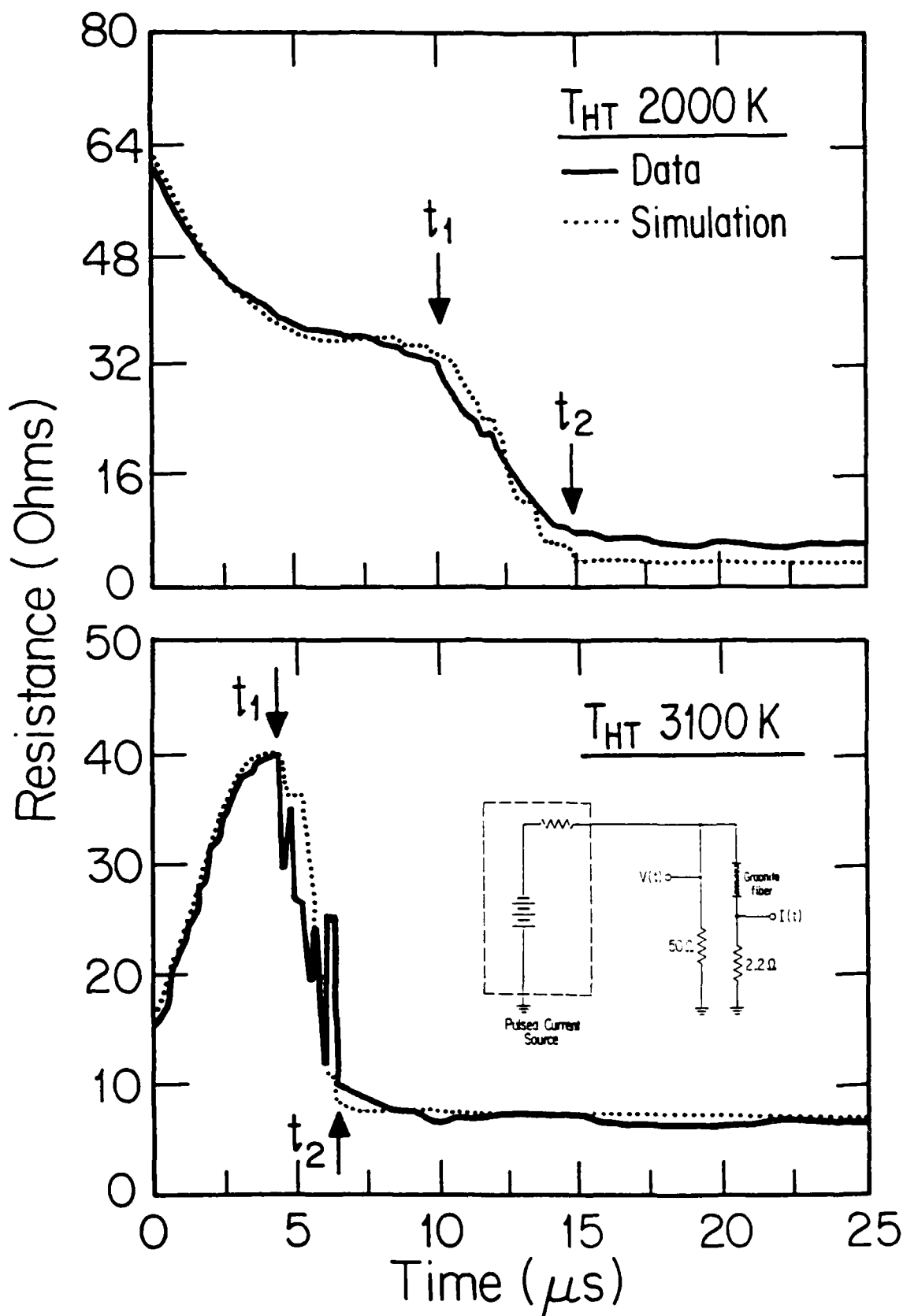


Figure 2: Time dependence of the resistance of two carbon fibers (prepared with different heat treatment temperatures) while heated by a 28 μsec current pulse. The schematic for the experimental arrangement used to heat and melt the graphite fibers is shown in the inset to the lower trace [14]. The dotted curves represent the results of a computer simulation based on solution to the heat flow equation.

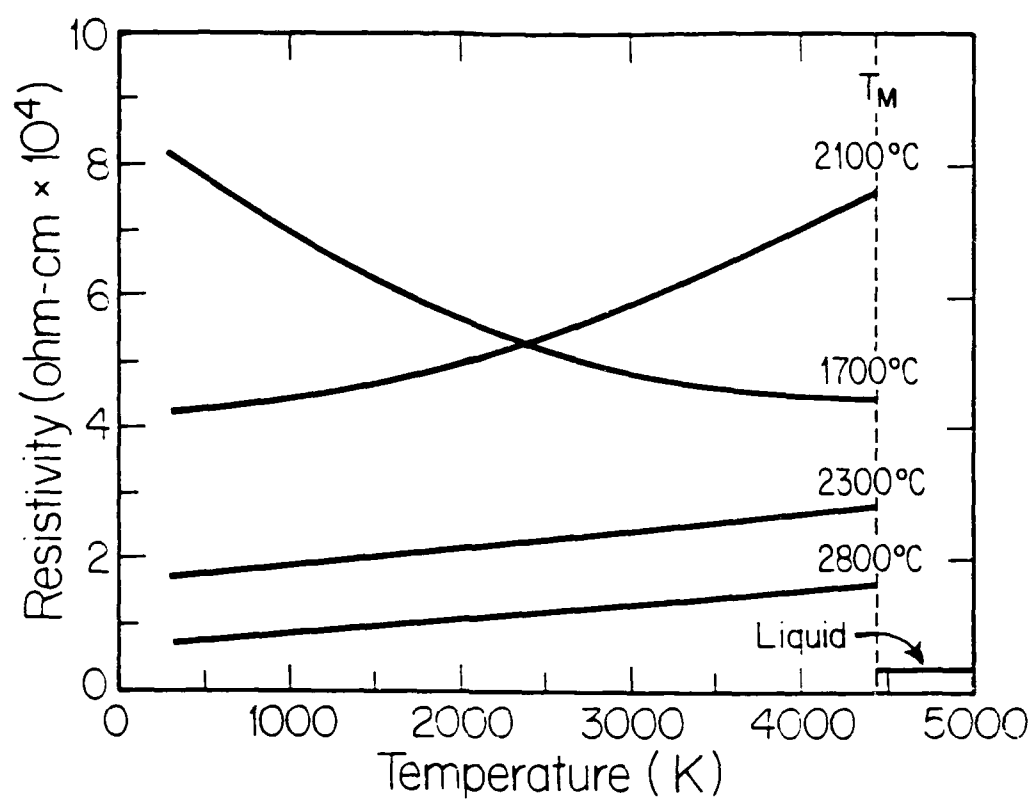


Figure 3: The electrical resistivity versus temperature for graphite fibers with $T_{HT} = 1700, 2100, 2300, 2800^\circ\text{C}$. The measured electrical resistivity for liquid carbon is shown. Note that the electrical resistivity for the fiber with $T_{HT} = 1700^\circ\text{C}$ is the only one characteristic of an activated conductivity in the solid state [14].

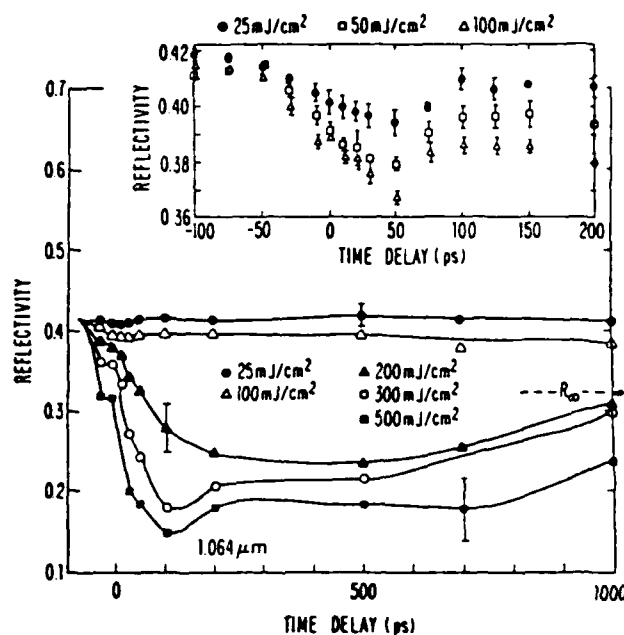


Figure 4: Transient reflectivity measurements using pulsed laser heating and a pump/probe detection technique. The pump and probe were provided by a 20 psec pulse from a Nd:YAG laser operating at the 532 nm harmonic and the delay time between the pump and probe was varied. The inset shows the short delay time data for low laser energy densities [5].

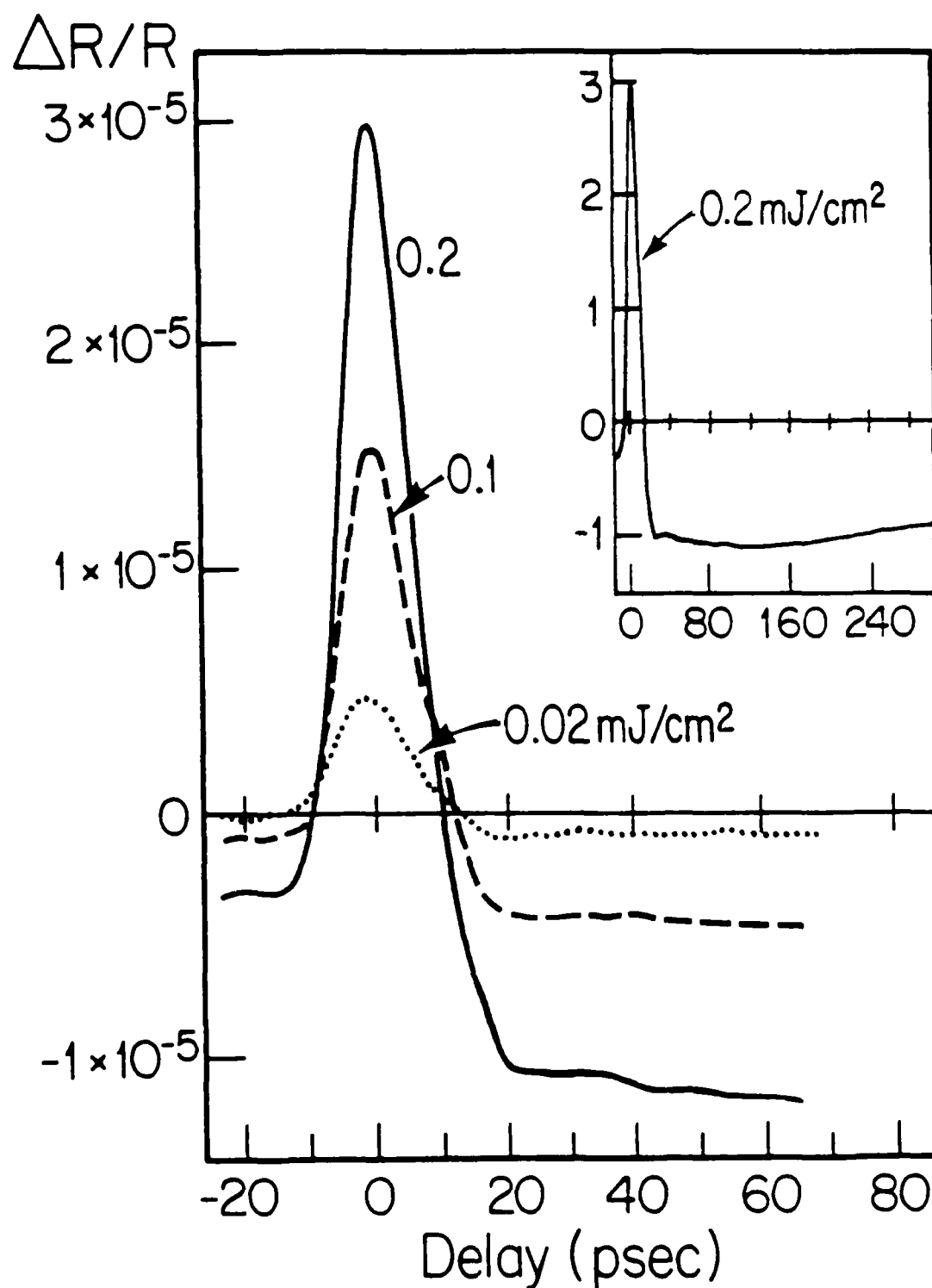


Figure 5: Time dependent reflectivity of highly oriented pyrolytic graphite heated by a 5 psec laser pulse [633 nm] at laser energy densities far below the threshold for melting. The probe laser is at 592 nm. The inset shows the reflectivity response for the 0.2 mJ/cm² laser energy density over a longer time scale [14].

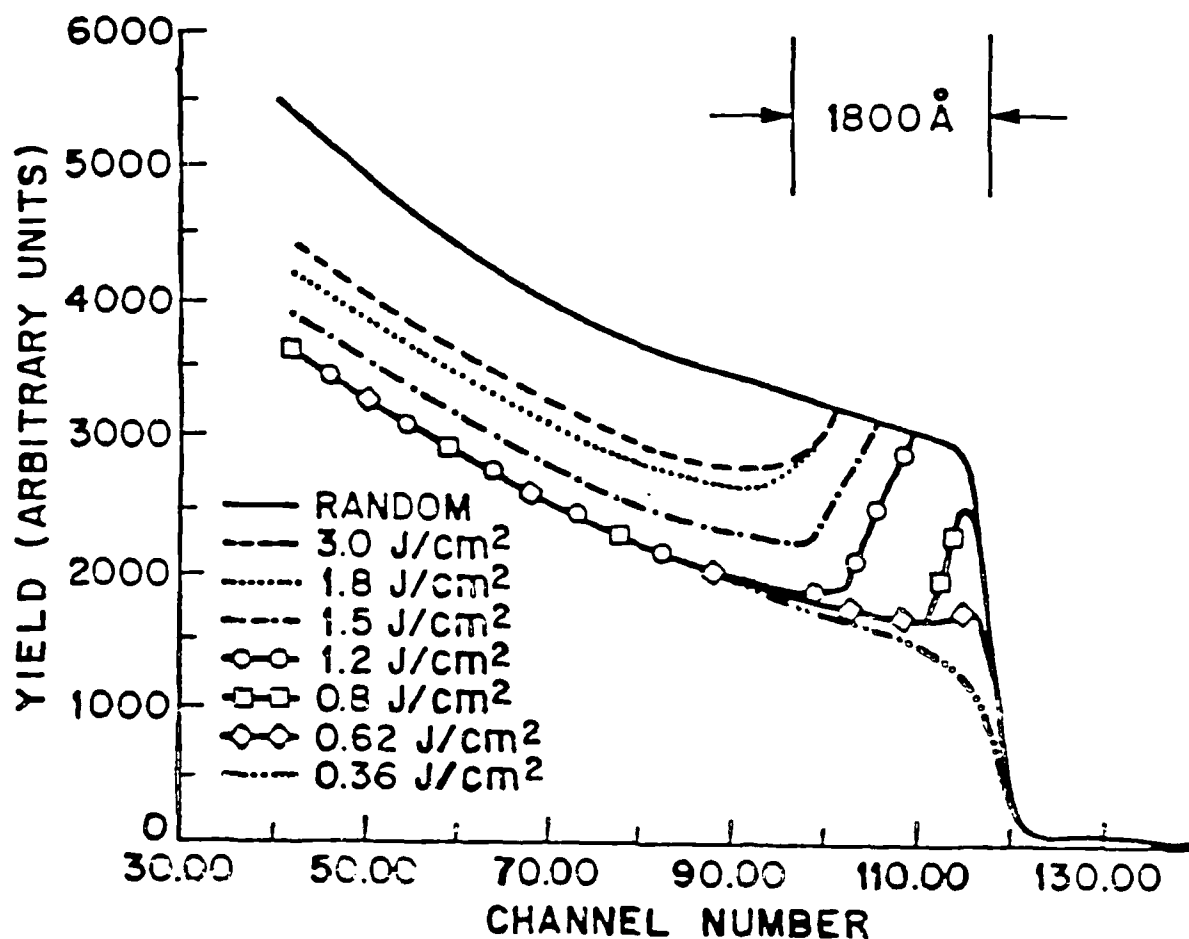
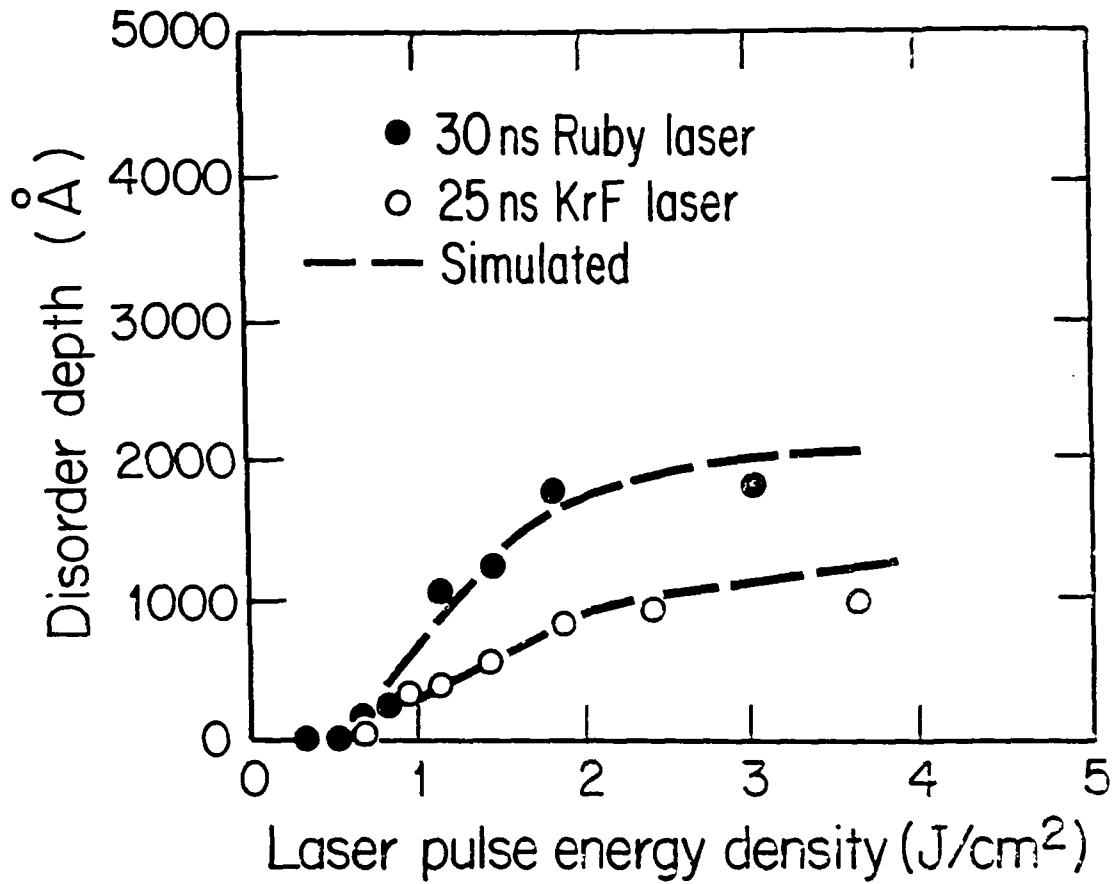


Figure 6: (a) Rutherford backscattering/ion channeling spectra for 30 nsec pulsed ruby laser irradiated graphite (694 nm). The onset for formation of the disordered layer occurs for a laser energy density of 0.6 J/cm² [4].



(b) Summary of the results of ion channeling spectra on graphite for a 30 nsec pulsed ruby (694 nm) laser and a 25 nsec pulsed KrF (248 nm) laser. The points are experimental and the fits (dashed lines) are made by solution of the heat equation [4,13,16].

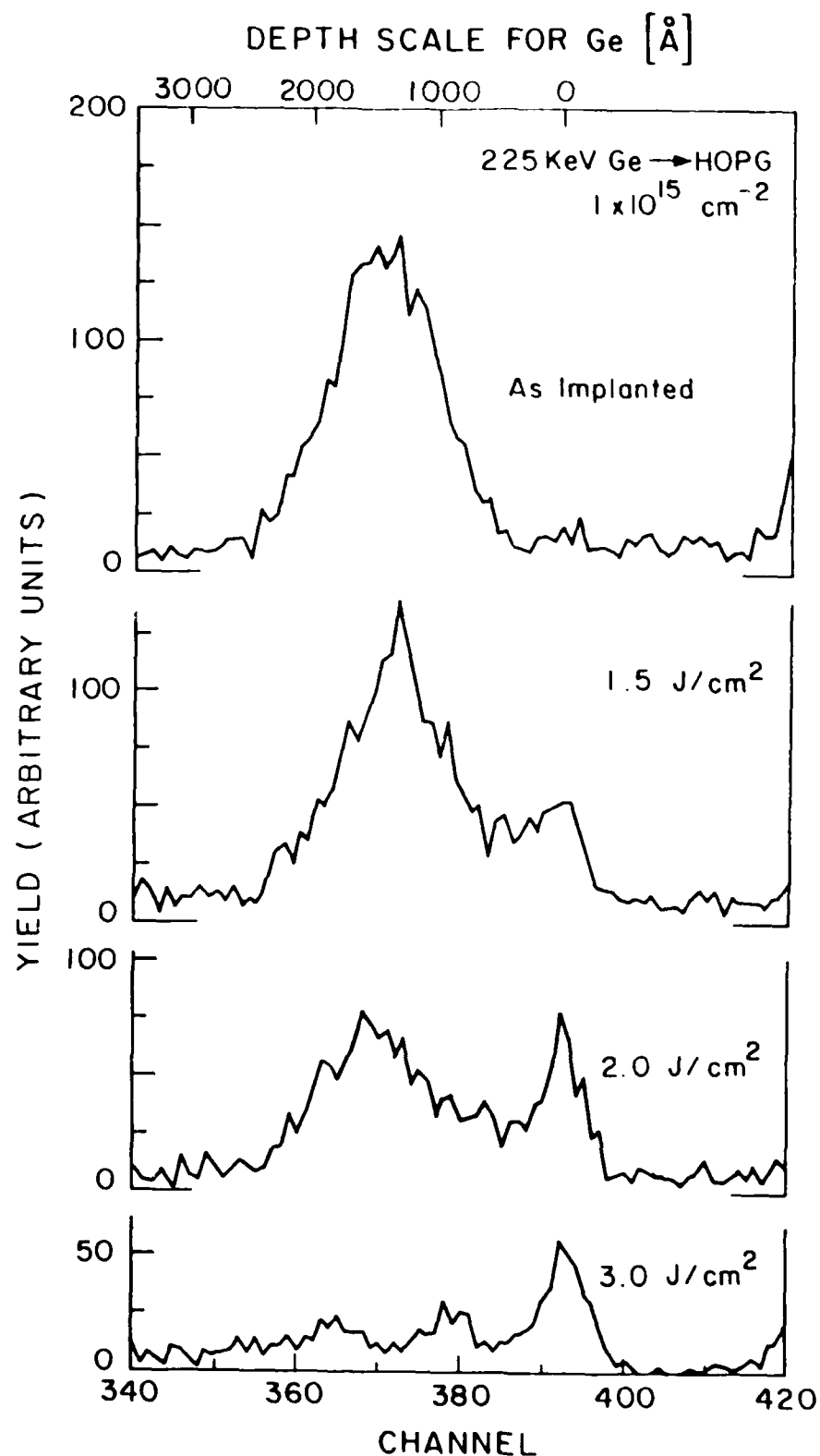


Figure 7: Plot of the Rutherford backscattering yield vs. depth (channel number) showing the redistribution of ion implanted germanium in pulsed laser irradiated graphite for several laser energy densities. Note the movement of impurities to the surface using the depth scale shown on the top of the figure [23].

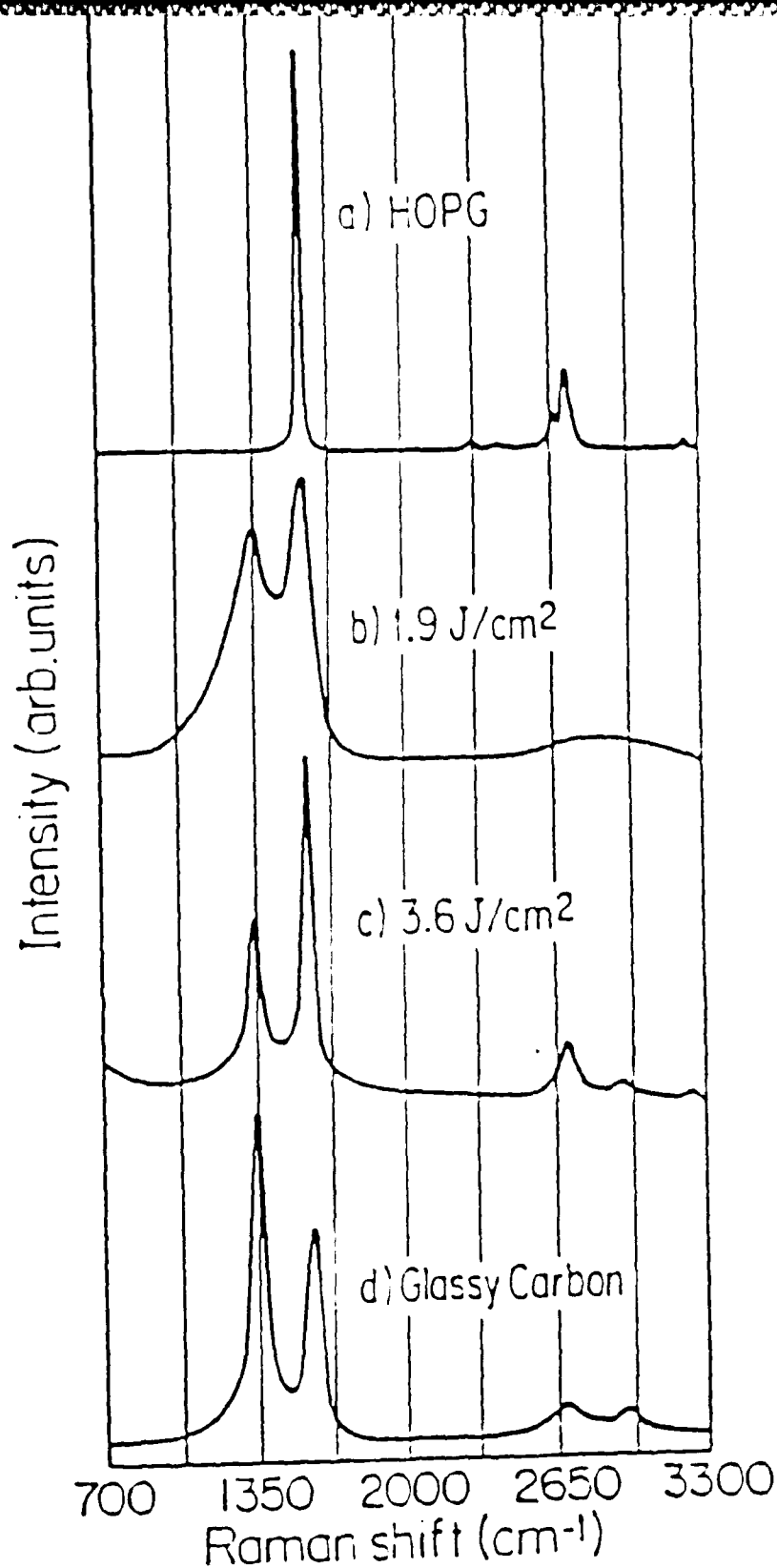


Figure 8: Raman spectra for pulsed irradiated graphite. The spectrum in (a) is for the first and second order Raman peaks in graphite prior to the laser pulse. The spectra in (b) and (c) are the first and second order Raman spectra for graphite irradiated with an energy density of 1.9 J/cm^2 and 3.6 J/cm^2 from a 30 nsec pulsed ruby laser, respectively. For comparison, the spectrum in (d) is for glassy carbon, a disordered graphite with a small crystallite size.

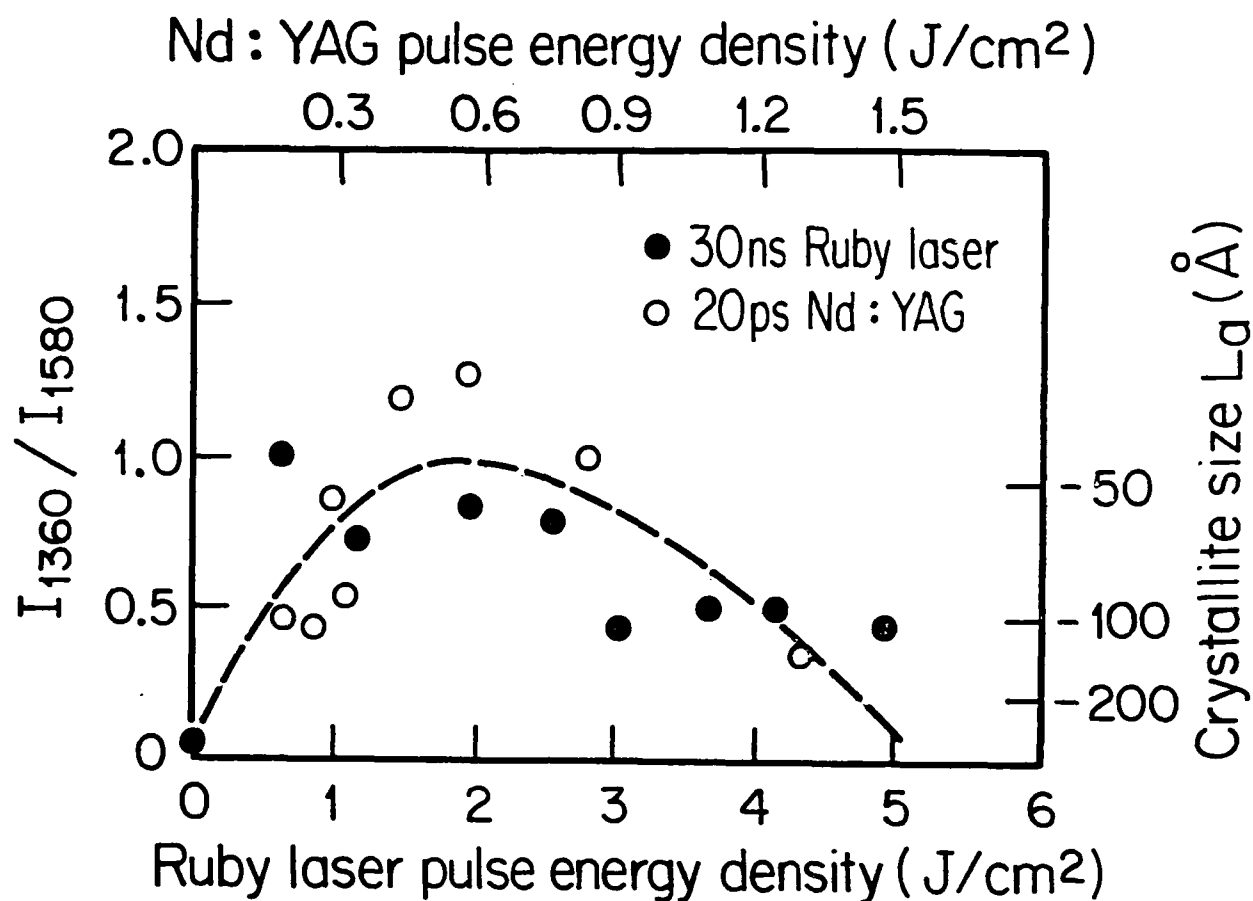


Figure 9: A summary of measurements of the Raman intensity ratio I_{1360}/I_{1580} made with a 20 psec Nd:YAG (532 nm) pulsed laser and a 30 nsec ruby (694 nm) pulsed laser for the laser energy densities shown on the upper and lower scales. Note the relation between I_{1360}/I_{1580} and the in-plane crystallite size L_a shown on the right hand scale [27].

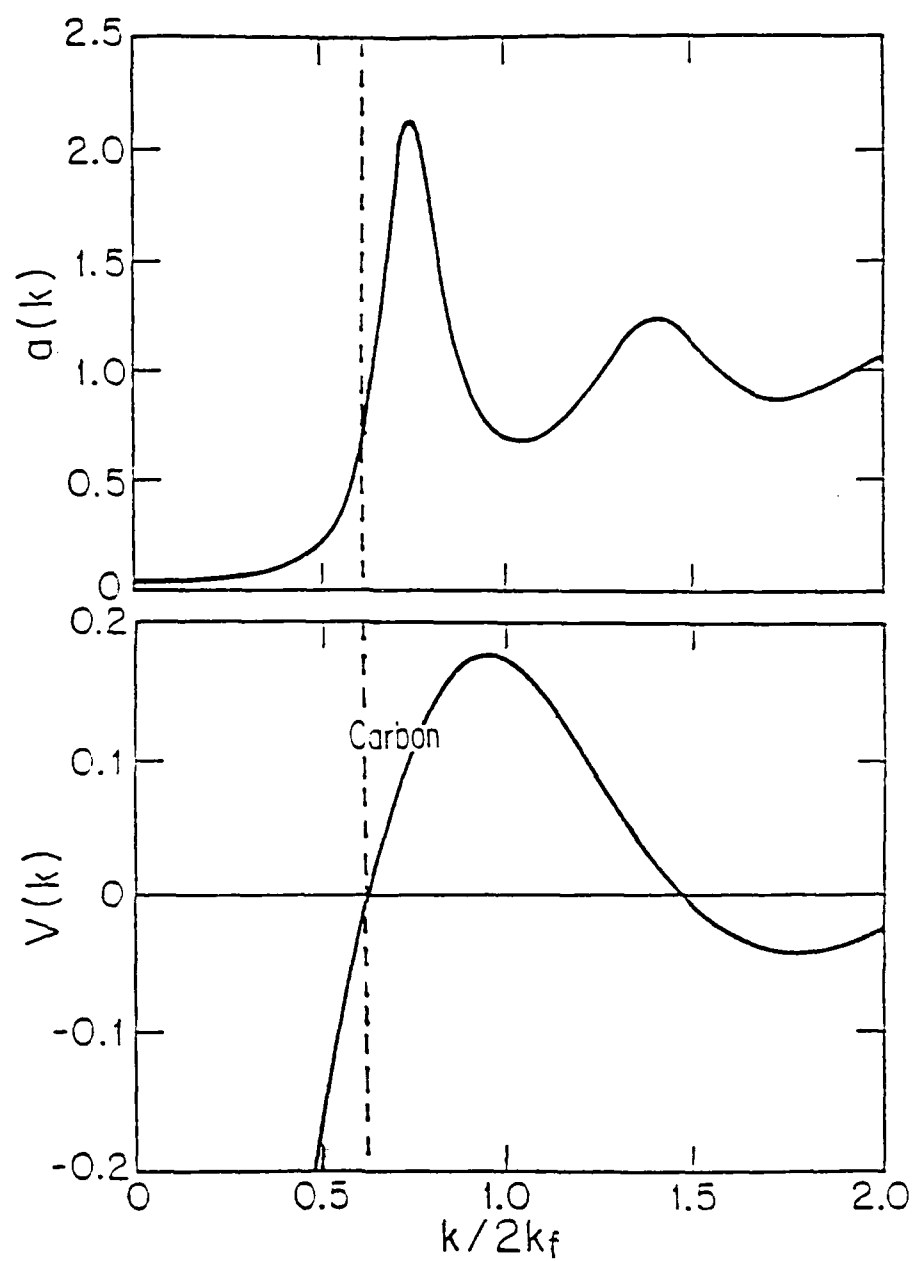


Figure 10: The liquid structure factor $a(k)$ and the pseudopotential function $V(k)$ for a metallic liquid carbon phase [13]. The dashed line denotes the k value of the node in $V(k)$.

END

DATE

FILMED

5-88

DTIC